







Simulation of current-driven magnetisation switching in nanopillars with Perpendicular Shape Anisotropy

Natalia Boscolo Meneguolo¹ ,* Daria Gusakova¹ , Jean-Christophe Toussaint² ,
Mouad Fattouhi¹ , Ioan-Lucian Prejbeanu¹ , and Olivier Fruchart¹ 
¹*Univ. Grenoble Alpes, CEA, CNRS, Grenoble INP, SPINTEC, 38000 Grenoble, France* and
²*Univ. Grenoble Alpes, CNRS, Institut Néel, 38000 Grenoble, France*
(Dated: March 20, 2025)

The Perpendicular Shape Anisotropy Spin Transfer Torque Magnetic Random Access Memory (PSA-STT-MRAM) is a recent concept proposed to maintain the thermal stability of standard MRAM at small diameters, considering thick vertical pillars as the free layer. In order to explore the specific physics of PSA-STT-MRAMs expected in relation with their three-dimensional nature, we have performed simulations combining a micromagnetic model coupled self-consistently with spin-dependent transport equations. The 3D shape induces flower states at the upper and lower surfaces. Besides, the field-like component of STT is found to be larger than in standard MRAMs, suggesting that it needs to be considered. The combination of both effects leads to the efficient excitation of edge ferromagnetic resonance modes, playing a key role in magnetisation reversal. These results highlight features of 3D nanomagnetic systems, largely disregarded so far, which need to be considered to optimise PSA-STT-MRAM to be a competitive solution for technological implementation.

Keywords: Micromagnetism, Finite Element Method, Simulations, 3D nanomagnetic system, spin accumulation, STT, MRAM

I. INTRODUCTION

Over the recent years the interest in 3D nanomagnetism has steadily grown, with both fundamental and applied interests [1]. On one side 3D nano-objects allow the existence and the tailoring of new magnetic properties related to curvature and finite size: effective anisotropy and Dzyaloshinskii–Moriya interaction, static or dynamic chiral effects etc. On the other side, these may find practical application that take advantage of the effects specific to 3D nanomagnetism [2]: increased stability against thermal excitation, nano-oscillators with tunable frequency, flexible nano-membranes with tunable magnetic properties, magnetic interconnects able to merge memory and logic units [3, 4] etc. The third dimension also opens new prospects for spintronics [5]. An example is networks of magnetic nanowires [6, 7], which may be advantageous when thinking about 3D integrated magnetic devices for neuromorphic applications and in-memory computation, thanks to their enhanced connectivity.

The Perpendicular-Shape-Anisotropy Spin-Transfer-Torque Magnetic Random Access Memory (PSA-STT-MRAM) is another example making use of 3D concepts for applied spintronics [8, 9]. The main advantage of this new concept for MRAMs is to boost the thermal stability of the free layer of the Magnetic Tunnel Junction (MTJ, the unit cell of the MRAM) at diameters down to a few nanometers, providing a scalable solution to the foreseen bottleneck of standard perpendicular MTJs be-

low typically 25 nm. This is achieved thanks to the drastic increase in thickness of the MTJ free layer, taking the form of a vertical nanopillar, therefore, a 3D nanomagnetic system. Unfortunately, some drawbacks stem from the increase of the free layer thickness. We withstand namely to the high writing critical voltage and slow writing time. Indeed, in an MTJ the spin-transfer torque is mostly an interfacial effect, therefore moderately efficient to switch the magnetisation of a 3D system. To address this problem, slicing the free-layer pillar into a multi-layer stack has been proposed [10]. However, while this solution indeed reduces the current required for writing, it relies on the standard fabrication route of deposition plus aggressive etching routes [8, 9], so that it suffers from large device-to-device distributions. Also, the required physical vapor deposition cannot be implemented in microelectronics vias, that would provide a natural route for high-density networks [11]. Therefore, simulation of current-driven magnetisation switching in nanopillars remains relevant to identify their dynamics and identify routes to improve it. Such simulations have already been conducted [8, 12], in which the so-called adiabatic component of spin-transfer torque was implemented as an interfacial term, such as is routinely done in conventional thin free layers of MRAM [13].

In this article we propose to refine these approaches, considering two ingredients that we believe are crucial to properly describe a 3D spintronic-nanomagnetic system. To do so, we evaluate explicitly and consider self-consistently the spin accumulation in the entire nanopillar. We employed a Finite-Element Method micromagnetic solver, to faithfully describe the curved shape of a nanopillar [14]. The structure of this article is the following: in section II we describe the methods, presenting the main aspects of the `feeLLGood` micromagnetic solver:

* natalia.boscolomeneguolo@cea.fr

the Finite Element Method used for the meshing procedure, the physics underlying the modeling of the magnetisation dynamics, focusing namely on the spin accumulation computation. In section III we report the main simulation results, starting from the specificities related to the mesh size, continuing with the magnetisation behaviour at the edges of the pillar, and finishing with spin accumulation and the link between reversal mode and magnitude of the injected current density. In section IV we draw conclusions and perspectives.

II. METHODS

A. Finite Element Method micromagnetic solver

There are a number of ways to discretise the specimen in micromagnetic simulations, *e.g.*, the Finite-Difference Method (FDM), the Finite-Volume Method (FVM) and the Finite-Element Method (FEM) [15, 16]. In the present work we use `FeeLLGood`, a finite-element 3D micromagnetic solver developed over the past two decades at Institut Néel and SPINTEC in Grenoble[14]. The FEM method is very flexible and suited to discretize complex and curved shapes. In practice, the specimen volume is meshed with GMSH, an open source 3D finite element mesh generator [17]. We chose a mesh of unstructured type, meaning that it has not a uniform pattern. More precisely, the discretization is obtained by first meshing the surface through the boundary recovery algorithm [18], while the mesh points inside the volume are added through a 3D version of the Delaunay algorithm [19].

B. Zhang-Li-like STT

The description of the dynamics of the system results from solving the Landau-Lifshits-Gilbert (LLG) equation:

$$\frac{\partial \mathbf{m}}{\partial t} = -\mu_0 \gamma (\mathbf{m} \times H_{\text{eff}}) + \alpha \left(\mathbf{m} \times \frac{\partial \mathbf{m}}{\partial t} \right). \quad (1)$$

In equation (1) $\gamma > 0$ is the gyromagnetic ratio, μ_0 is the vacuum magnetic permeability, \mathbf{m} the unitary magnetisation (the value of the magnetisation normalized by the spontaneous magnetisation M_s), H_{eff} is the effective field and α is the Gilbert damping factor. More information can be found in Ref.[20–22]. In addition to the LLG equation (1), we consider also the impact of the spin torques (STT) in the system. In order to avoid losing generality, the STT impact is taken into account by adding an extra term to (1):

$$T_{\text{STT}} = \frac{1}{\tau_{\text{sf}}} (\mathbf{m} \times \mathbf{s}) \quad (2)$$

T_{STT} accounts for the mutual interaction between magnetisation and the spins of conduction electron. Historically, the STT torque description has been simplified for a bilayer, exploiting the so-called LLGS equation (where S stands for Slonczewski):

$$\left(\frac{\partial \mathbf{m}}{\partial t} \right)_{\text{STT}} = -\gamma \mu_0 \eta_{\text{STT}} \frac{\hbar J}{2 |e| M_s t} \mathbf{m} \times (\mathbf{m} \times \mathbf{m}_{\text{pol}}) + \gamma \mu_0 \eta'_{\text{STT}} \frac{\hbar J}{2 |e| M_s t} (\mathbf{m} \times \mathbf{m}_{\text{pol}}). \quad (3)$$

In equation (3) η_{STT} represents the STT efficiency, whose value can be estimated from the tunnel magnetoresistance of the devices, \hbar is the reduced Planck constant, e is the electron charge, M_s is the value of the spontaneous magnetisation of the material, J is the current density injected in the system, t is the thickness of the magnetic free layer, \mathbf{m} is the unit vector for magnetisation and \mathbf{m}_{pol} is the unit vector for magnetisation in the reference layer which we assume to be fixed, separated by a tunnel barrier from the free layer considered. There are two spin torque terms in the right-hand side of Eq.(3). The first one is the so-called Damping-Like component (DL, also called in-plane), that drives magnetisation towards the local effective field. The second term is the Field Like component (FL, also called out-of-plane), which induces magnetisation to precess around the local effective magnetic field. Usually, in 2D systems the FL component is neglected, since it has been shown to not play a major role in the reversal mechanism [13]. This corresponds to the formalism introduced for the first time by J. Slonczewski in 1996 [23].

Another conceptual way to describe the STT is to consider four contributions in total: two of them related to the change in time of magnetisation and the other two related to its variations in space. The time-related contributions can be accounted for by redefining the gyromagnetic ratio γ and the Gilbert damping factor α . The space-related terms instead, describe two main interactions: first, the ballistic motion and all the adiabatic processes of conduction electrons; second, the non-adiabatic spin torque that are consequences of the spatial mistracking of spins between conduction electrons and local magnetisation. This description is the Zhang-Li one, introduced in 2004 by S. Zhang and Z. Li [24]. `FeeLLGood` relies on this Zhang-Li-like description of the STT.

C. Spin accumulation

Spin-transfer torques result from spin accumulation, *i.e.*, an out-of-equilibrium imbalance of up and down spins of the conduction electrons. There can be different implementations of STTs. When dealing with standard MRAM with perpendicular magnetization, which have an ultrathin thin layer, one generally assumes that the spin accumulation is uniform across the free layer, with

an effective value that can be derived from experimental data obtained through spin-pumping and spin Hall effect measurements [25]. However, this approach may be challenged when dealing with 3D structures. An ersatz consist in considering an effective interfacial STT, *e.g.*, decaying away from the interface in an effective exponential way[12]. However, this choice can also be questionable, not considering the precessional effects of the spins over this length scale. For this reason, here we consider the full spatial variation of spin accumulation in the nano-pillar, which is calculated at each iteration of the solving protocol by coupling the LLG equation (used for the determinations of the dynamics of the system) to diffusive transport equations. In this picture, the spin accumulation \mathbf{s} induces an additional contribution to the effective magnetic field acting on the local magnetisation, with units $\text{A} \cdot \text{m}^{-1}$.

The system of equations that have to be solved to determine the spin accumulation \mathbf{s} is the following [26]:

$$\text{div } \mathbf{j} = C_0 \mathbf{E} = -\text{div } C_0 \mathbf{grad } \mathbf{V} = 0, \quad (4)$$

$$\text{div } \mathbf{Q}_i^s = -\frac{s_i}{\tau_{\text{sf}}} - \frac{(\mathbf{s} \times \mathbf{m})_i}{\tau_{\text{sd}}}. \quad (5)$$

Eq.(4) expresses the total current \mathbf{j} resulting from the local electric field $\mathbf{E} = -\mathbf{grad } \mathbf{V}$, C_0 being the electric conductivity [$\Omega^{-1} \cdot \text{m}^{-1}$]. In our convention, positive current \mathbf{j} means current flowing through the tunnel barrier to the free layer, which means, electrons flowing from the free layer through the tunnel barrier. Spin has the meaning of magnetic momentum, *i.e.*, is parallel to the corresponding layer magnetisation. Eq.(5) is a conservation equation, expressing the grounds for the variation of local spin accumulation, resulting either from the spatial variation of the spin-polarized current \mathbf{Q}_i^s on the left-hand side, or spin flip and spin precession, on the right-hand side. In this context, i refers to the spatial direction ($i \in \{x, y, z\}$), τ_{sf} is the spin-flip characteristic time, and τ_{sd} is the sd coupling characteristic time. Note that $\mathbf{Q}_i^s = \mathbf{j} \cdot P_{u,z}$ with $P_{u,z}$ the polarisability ratio, a parameter related to the polarisation of the electrical current flowing in the bulk. In our simulations we simplify the picture by considering that $P_{u,z}$ has the same value as β , a parameter used to express the polarisation of conduction electrons injected in the ferromagnet, and known as the polarisability rate.

When describing spin accumulation we have to consider the surroundings and boundary conditions for the magnetic elements. On the side of the tunnel junction we set the boundary condition of a uniform areal density of current, with spin polarization $\beta = 0.57$. On the other side we describe the spatial variation of spin accumulation in the non-magnetic metal contact, with continuity of both the current density and chemical potential at the interface [27]. In this framework, to hold equations

(4) and (5) requires no spin accumulation discontinuity at the interface and an equal normal component of the spin polarized current (the needed stimulus to trigger the magnetisation reversal). The length of the non-magnetic electrode is set to 60nm, and a uniform voltage is applied as boundary condition of the electrode.

We will see in sec.III that considering spin accumulation instead of interfacial STT indeed leads to drastic quantitative difference in the case of a 3D nanomagnetic object.

D. Material parameters

The magnetic material of the free layer is FeCoB and that of the metal is Cu. TABLE I lists the parameters used in the simulations.

TABLE I. Material parameters used in the simulations. If not stated otherwise the parameters apply both to the magnetic system (MS) and the non-magnetic electrode (NM).

Parameter	Symbol	Value
Saturation magnetisation of MS	M_s	1 MA/m
Exchange constant	A_{ex}	1.5×10^{-11} J/m
Uniaxial anisotropy	K_u	0.96×10^6 J/m ²
sf decay length	l_{sf}	5 nm
sd decay length in MS	$l_{\text{sd,MS}}$	1 nm
sd decay length in NM	$l_{\text{sd,NM}}$	0 nm
Electric conductivity	C_0	$4.0 \times 10^6 / (\Omega \cdot \text{m})$
Number of atoms	N_0	$1.344 \times 10^{47} / (\text{J} \cdot \text{m}^3)$
Polarisability rate	β	0.57
Polarisability ratio	$P_{u,z}$	0.57

III. RESULTS

In this section, we highlight simulation and physical features specifically related to the consideration of a 3D nanosystem, which do not show up when considering the thin free layer of a standard MRAM.

A. Meshing

A usual concern in micromagnetics is the choice of the meshing size. To investigate this aspect in the present situation, we consider the demagnetising factors N_i ($i \in \{x, y, z\}$). These are important micromagnetic parameters as they determine the internal field for macrospins, and thus their precession frequency. Besides, the stability parameter Δ of a PSA-MTJ is directly related to the energy barrier of the system E_b , itself linked to N_i .

Starting from the values of the simulated demagnetising energies E_d for a uniformly-magnetised state, the demagnetising factors N_i are computed as:

$$N_i = \frac{2E_{d,i}}{\mu_0 M_s^2 V} \text{ where } i \in \{x, y, z\}. \quad (6)$$

Since the sum of the three demagnetising factors along the main directions is equal to one ($N_x + N_y + N_z = 1$) and given that for a cylinder $N_x = N_y$, we may restrict the study of the numerical evaluation of E_d in one direction. In principle, the results should be the same no matter the considered direction. Nevertheless we computed ($N_x - N_z$) twice, starting either from $E_{d,x}$ or $E_{d,z}$. The results are reported in TABLE II for different vertical aspect ratios $AR = t/D$ of the magnetic cylinder, with t the thickness of the free layer and D its diameter.

TABLE II. Demagnetising factors of cylinders of different aspect ratio calculated from the simulated value of either $E_{d,x}$ or $E_{d,z}$ for uniform magnetisation, with subsequent relative error ϵ_{xy} in the ($N_x - N_z$) difference value. The average size of the edge of a tetrahedron constituting the mesh is of 4 nm for all four cases.

AR	$(N_x - N_z) _{E_{d,x}}$	$(N_x - N_z) _{E_{d,z}}$	ϵ_{xy}
1	0.02	0.065	70 %
1.5	0.14	0.161	15 %
2	0.2	0.245	18 %
3	0.296	0.308	4 %

The relative error in TABLE II is computed as:

$$\epsilon_{xy} = \frac{(N_x - N_z) |_{E_{d,x}} - (N_x - N_z) |_{E_{d,z}}}{(N_x - N_z) |_{E_{d,x}}} \quad (7)$$

The relative error for the cylinder with AR 1 is striking. It reaches about 70%, while it drops sharply for larger AR. This can be understood as 1 is an AR for which the magnetisation orientation in the system is close to the transition from out-of-plane to in-plane for lower values, so that small errors translate into large differences. The error drops to 26% upon halving the average length of the edge of tetrahedron unit cells to 2 nm. This issue of large relative error is specific for a 3D nano-object, as for the flat shape of standard p-MRAM the x and z demagnetising coefficients are very different one from another, so that errors in the difference are low. This shows that one needs to pay extra attention to mesh size refinement in 3D.

B. Flower state

FIG. 1 shows the micromagnetic state in a pillar with vertical aspect ratio 1, after relaxation taking from uniform magnetisation as the starting point. There are deviations of magnetisation from the uniform state at the edges of the structure, for both the upper and lower surfaces, which is called a flower state[28]. This situation results from the divergence of dipolar fields at edges and

corners[29], whose cost in terms of dipolar energy is decreased by rotating magnetisation towards the diagonal to the edge, at the expense of exchange energy[30]. In our case the angular deviation from the z -axis at the very edge is about 9° , while at the center of both surfaces magnetisation is aligned with the z -axis. The occurrence of the flower state is specific to a 3D system, with a size larger than the dipolar exchange length. In the thin free layer of an MRAM the dipolar effects from top and bottom surfaces overlap and cancel each other at the length scale of the layer thickness, leaving it in a uniform state. We will see in sec.III D that this has a direct and specific effect on current-driven magnetisation dynamics.

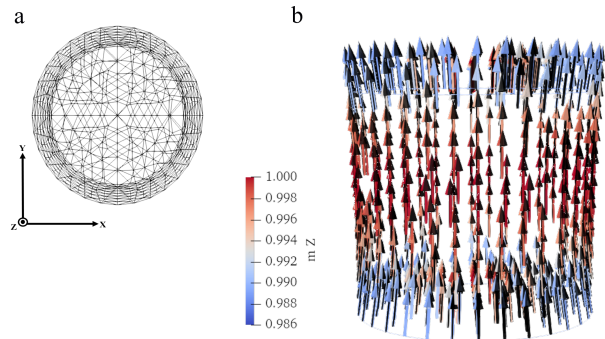


FIG. 1. (a) Representation of the FEM mesh used to discretize a pillar with 20 nm height and 20 nm diameter. (b) Relaxed micromagnetic state. The arrows represent the direction of the local magnetic moments. In order to highlight the flower-state a color scale indicates the value of the z component of the unit magnetisation.

C. Spin accumulation

FIG. 2 illustrates the simulated spin accumulation s in the magnetic and the metal parts for a structure with $AR = 1$. The blue and red curves represent the spin accumulation for the parallel and anti-parallel states, respectively. As mentioned in the methods part, the so-called spins are parallel to the associated magnetic moment, and electrons flow in the direction opposite to the charge current. FIG. 2 is drawn for positive current, *i.e.*, electrons are injected from the free layer into the polarized layer. Several aspects are worth mentioning. First, spin accumulation occurs not only at the tunnel barrier, but also at the interface with the normal metal. In a metal/ferromagnet/metal stack this would induce an antidamping-like torque at the interface where the electrons enter the ferromagnet due to the accumulation of spins antiparallel to magnetisation, and a damping-like torque at the interface where the electrons leave the ferromagnet, due to the accumulation of spins parallel to magnetisation. This picture is consistent with the generalized Landau-Lifshitz-Gilbert-Slonczewski equation[31],

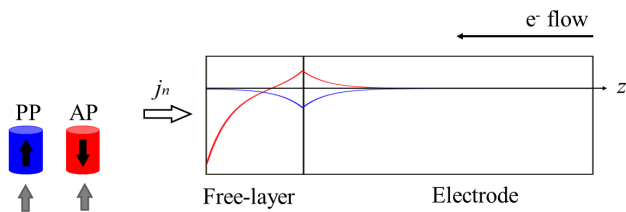


FIG. 2. Spin accumulation in the magnetic layer and metal contact for a free layer of 20 nm both thickness and diameter. The current density injected through the tunnel barrier is $j = 5 \times 10^{12}$ A/m² with a polarisability ratio of the injected current $P_{u,z} = 0.57$. The vertical axis represents in arbitrary units the cross-sectional-average of the z component of spin accumulation. The situations for the parallel state of uniformly-magnetised polarizer and free layer are depicted in blue and red, respectively. The bottom-left corner schematic illustrates the geometry, of the parallel (PP) and anti-parallel (AP) configurations with positive charge current, gray arrows representing the magnetisation direction in the reference layer and the black arrows the magnetisation direction in the free layer.

if the gradient of magnetisation close to the interfaces is considered: the flow of electrons promote a larger angular deviation at the interface through which they enter the mostly uniformly-magnetized material, and a lower angle at the interface through which they exit the material. Second, STT is not localized at interfaces, but decays progressively away from these at the length scale of the spin diffusion length, such as described by the Valet-Fert model for giant magneto-resistance in the current-perpendicular-to-plane geometry[27]. This length scale is a few nanometers, comparable to magnetic length scales such as the dipolar exchange length, and therefore liable to efficiency couple to non-uniform magnetisation distributions such as the flower state described previously. Third and as a consequence of the previous statement, the height of the pillar has a direct impact on the value of spin accumulation, depending whether it is smaller or larger than the spin diffusion length. The former case is that of a standard MRAMs with a thin free layer, for which the Valet-Fert-like accumulations with opposite signs overlap and largely cancel each other, leaving the polarisation of the injected current as the main driving force for spin accumulation, independent of the magnetisation direction in the free layer. For the latter case, which is the situation of study here, the magnitude of spin accumulation at the tunnel barrier depends strongly on the direction of magnetisation of the free layer.

Another difference between the model of effective STT and the one of spin accumulation is that the ratio of damping-like and field-like torques is a direct output of the latter. To disentangle both we compute the amplitude of STT versus the misalignment angle of magnetisation with the z -axis, while keeping the polarizer fixed (FIG. 3). The results for a 2D-like system (cylinder

of 1 nm \times 20 nm) and a 3D-like one (cylinder of 20 nm \times 20 nm) are numerically computed, taking into account the value of the torque in reduced units:

$$\mathbf{T} = \frac{1}{\tau_{sd}} \frac{\mathbf{s}}{M_s} \times \mathbf{m}. \quad (8)$$

(FIG. 3) shows that while in the case of the 2D system the DL component dominates over the FL, as has been pointed out already [13], the two torques have a similar magnitude for the 3D system. How to link quantitatively the interfacial and bulk descriptions of STT requires further investigations, which lies beyond the scope of the present work. Nevertheless, the effects mentioned above already show qualitatively what is specific in a 3D nanomagnetic system, and expected to give rise to peculiar magnetisation dynamics, which we explore in the next paragraph.

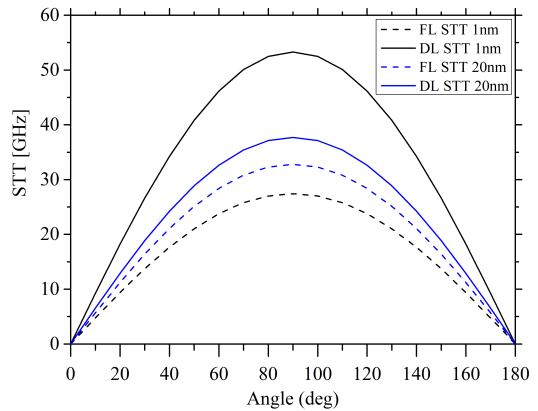


FIG. 3. STT components versus the angle of magnetisation in the free layer, with respect to the z -axis. Black stands for a 1 nm-thick system, while in blue stands for a 20 nm-thick system. FL torques are shown with full lines, DL torques with dotted lines.

D. Current-driven magnetisation reversal

If not stated otherwise, simulations are conducted for a cylinder having a diameter of 20 nm and a thickness of 20 nm, and a Gilbert damping factor $\alpha = 0.02$. The starting point of the simulation is uniform magnetisation with 1° misalignment with respect to z -axis, and abrupt flow of electric current from the start. Some of the values for the density of injected current are unrealistically-high for an experimental current through a tunnel barrier. However, covering a large range of stimulus allows us to highlight the various possible physics of 3D systems and their subsequent potentialities.

FIG. 4 shows the evolution of the z component of the average unit magnetisation m_z versus time, for five differ-

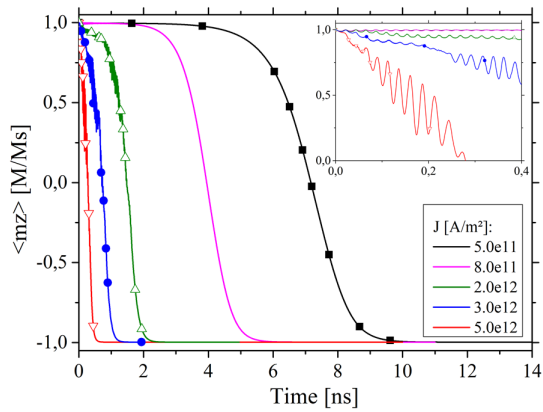


FIG. 4. z component of the unit magnetisation vs time for different values of injected electric current densities. The symbols refer to the time positions at which the snapshots reported in FIG. 6 were taken. The inset is a close-up view of the magnetisation evolution during the first 0.4 ns, highlighting oscillations.

ent values of injected current densities. $m_z = \pm 1$ means uniform magnetisation aligned with the z -axis upwards and downwards, respectively. Let us define two quantities to analyse the time scales of magnetisation reversal. A first time scale appearing on FIG. 4 is the time needed before a sizable change is noticeable. We define it arbitrarily when m_z reaches 0.9, which we call τ_i . It is sometimes called the incubation time, which for a macrospin reflects the gradual rise of the precession angle under the influence of the antidamping torque. It is usually strongly dependent on initial misalignment of the various magnetisation vectors, and on thermal and numerical noise. A second time scale is the time needed for the magnetic moment to go from mostly up to mostly down. We define it the time for m_z to go from +0.9 to -0.9, which we call τ_s . It is sometimes called the switching time.

FIG. 5 shows that up to current density of circa 10^{12} A/m², τ_i vary inversely linearly with the injected current. This behavior is expected[32] and observed[33] for the spin-transfer switching of a macrospin when the current exceeds the threshold for switching, simply reflecting the rate of transfer of angular momentum from spin accumulation to magnetisation[23]. The low slope is predicted to reflect in a logarithmic manner the initial misalignment angle θ_0 . τ_s also varies inversely linearly with injected current however with a larger slope, reflecting the larger reference angle, with cosine equaling 0.9.

However, two features suggest that the the magnetisation dynamics is not fully grasped by the macrospin picture. First, the inset of FIG. 4 shows that from the very first stages m_z oscillates during the incubation stage. The magnitude of oscillations increases sharply and non-linearly with the current density, and the frequency is more than one order of magnitude larger than

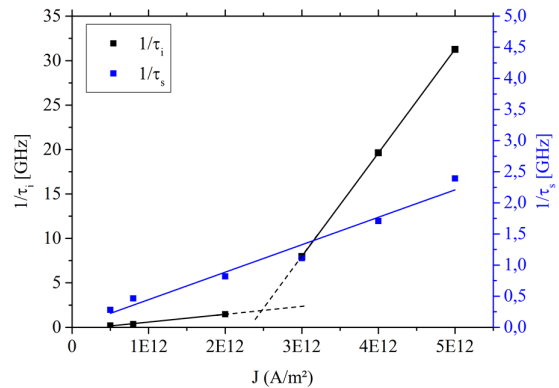


FIG. 5. Evolution of the characteristics inverse times $1/\tau_i$ and $1/\tau_s$ with injected STT current.

the macrospin gyroscopic precession (TABLE III). Second, a cross-over occurs at large current for the variation of inverse τ_i with applied current. In this regime, m_z departs linearly from saturation from the start of simulation, which again does not fit the standard picture of incubation of a macrospin. Note that as FIG. 4 does not display a plateau at mid-reversal one can probably rule out a mechanism of nucleation-propagation of domain wall[12, 34]. In the following paragraph we examine the magnetisation distributions during reversal to understand the microscopic reasons for these features.

FIG. 6 illustrates the magnetisation distribution at the surface of the magnetic cylinder during the reversal process, for different values of injected current. This series highlights a cross-over for nearly coherent reversal at low current density to incoherent at larger current density, with a threshold value comparable to the cross-over of $1/\tau_i$ in FIG. 5. Deviations from uniform magnetisation appear first at the edges of the interface with the tunnel junction, an effect most clearly visible for current density 3×10^{12} A/m² and higher. The linear decrease of m_z versus time observed for the highest current densities in FIG. 4 is explained by this non-uniform excitation mode, as the angle of precession can reach up to several tens of degrees and involve a macroscopic fraction of the volume of the cylinder. The excitation of these modes can be understood as spin accumulation is largest at this interface, and its effect is most efficient at the edges of the pillar due to the flower state. The efficient pumping of energy at these locations is confirmed by movies of the full magnetisation evolution, revealing the rise of precession of magnetisation turning the micromagnetic state periodically in flower-like, and leaf-like configurations with intermediate curling configurations with opposite chiralities (See supplementary material), with a frequency linked and thus explaining the oscillations of m_z (inset of FIG. 4). The frequency of precession f_{edge} is in the range 40 GHz to 45 GHz (TABLE III). This is fully

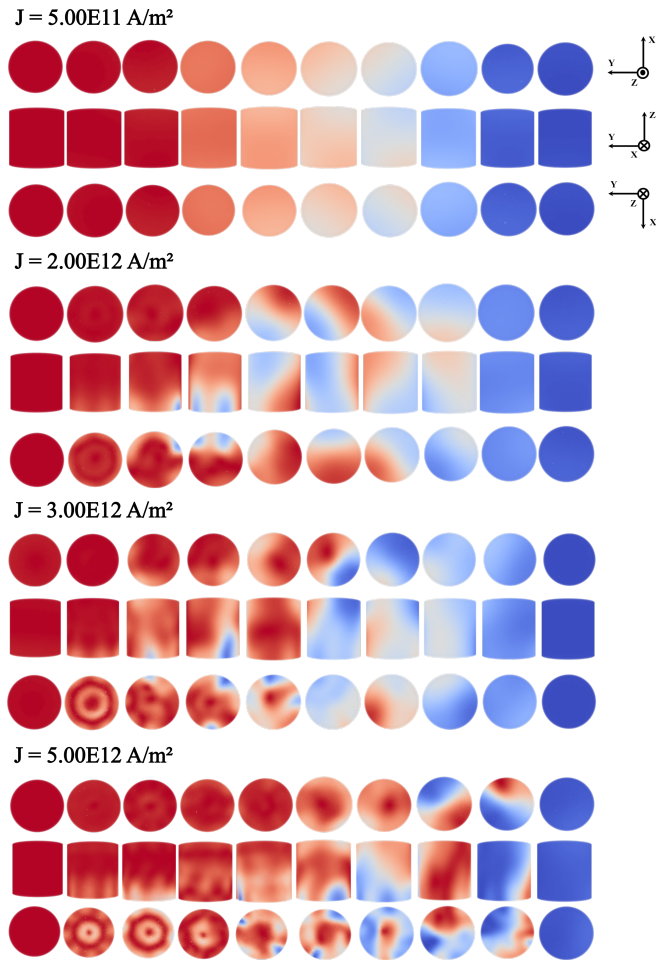


FIG. 6. Top, side and bottom views of magnetisation at the surface of a cylindrical volume of 20 nm thickness and 20 nm diameter over the current-driven switching process. Red corresponds to upward pointing magnetisation while blue corresponds to downward pointing magnetisation. From top to bottom are represented the results for increasing injected current densities. The different snapshots are taken for increasing time steps, starting from 0 ns. The time steps are not the same in the four cases but are spread over the switching time required by the specific configuration. The time steps at which the snapshots are taken are highlighted with symbols on the curves of FIG. 4.

inconsistent with the Kittel FMR formula of a macrospin in its own demagnetising field, related to $N_x - N_z$ [35]:

$$f = \frac{\gamma_0}{2\pi}(N_x - N_z)M_s, \quad (9)$$

which amounts to 1.23 GHz. This discrepancy and the localisation of the non-uniform mode at the edges of the cylinder makes clear that the local effective field involved is not the demagnetising field, but a combination of dipolar and exchange field involved in the flower state. The oscillation frequencies convert to ≈ 1.3 MA/m in terms of effective induction field. Given the fact that the radius of the cylinder is close to four times the dipolar exchange

length, this is exactly the range of frequency expected from the interplay of magnetostatics and exchange at this scale. Examining the evolution over time for a given current density is also interesting. It is clear that a breaking of symmetry is needed to reverse a macrospin, and this is what happens for the low current density. A breaking of symmetry is also required even in the case when an edge mode is the way that the system gets efficiently excited, for the large current densities. Indeed, magnetisation reversal via a perfectly-symmetry curling state requires the nucleation of a Bloch point on the axis of the cylinder[36], which is an energetically costly process[37]. Examining the edge modes over time, we notice that the breaking of symmetry takes the form of the mode changing progressively from a high azimuthal one to a low-azimuthal mode.

The change of azimuthal mode is associated with a transient state with low amplitude of oscillation, before oscillations are recovered however with a slightly larger frequency increase, see for instance FIG. 4 for current density 3×10^{12} A²/m.

Let us finally discuss the dependence of f_{edge} with applied current, which decreases by about 6 GHz from low current to 5×10^{12} A/m², so, amounting to 1.2 GHz · m²/A. Two phenomena may explain this dependence. The first possibility is the non-linearity of precession[38], due to the angle reaching several tens of degrees shortly before reversal for the largest current density. However, there is no clear gradual change of frequency during the increase of amplitude of oscillation for a given current density. The second possibility is the effective field arising from the field-like component of STT, the decrease being consistent with the expected antidamping effect. We may link this to the macrospin oscillations observed in the case of a damping torque. For a cylinder displaying 20 nm thickness and returning to equilibrium, the precession frequency changes from 2.13 GHz at zero injected current to 2.35 GHz for an injected current of 6.79×10^{11} A/m², *i.e.*, amounting to ≈ 0.3 GHz · m²/A. Both figures are therefore not consistent. In the end, there may be a contribution of both effects, non-linearity and field-like torque. The non-linearity of precession is also expected to induce a non-linear effect on the effective field-like torque, as it is the exchange between spin accumulation and magnetisation that connects the damping-like and field-like terms in our approach (see equation 2).

TABLE III. Frequency of oscillation of m_z derived from the inset of FIG. 4, expressed in GHz and in the equivalent effective field for gyrotropic motion H_{eff} .

Injected current	f_{edge}	Local H_{eff}
5×10^{11} A/m ²	46.22 GHz	1.313 MA/m
8×10^{11} A/m ²	46.10 GHz	1.310 MA/m
2×10^{12} A/m ²	43.70 GHz	1.240 MA/m
3×10^{12} A/m ²	42.31 GHz	1.203 MA/m
5×10^{12} A/m ²	40.38 GHz	1.148 MA/m

To conclude this part, edge modes are efficiently excited in 3D nanosystems, due to the combination of the flower state and larger field-like torque. This leads to pathways for magnetisation reversal which may deviate from the macrospin picture at large driving currents.

IV. CONCLUSIONS

We explored the details of spin-transfer-torque switching mechanism of 3D nanocylinders connected with a magnetic tunnel junction, and highlight the physical phenomena specific to the 3D situation, compared with thin elements such as found in standard MRAM. First, we showed that the explicit consideration of spin accumulation is necessary, being sizable in the vicinity of both interfaces, with the tunnel barrier and the metal lead. Besides, the field-like term is comparable with the damping-like one, contrary to the 2D case. This, combined with the flower state naturally occurring in a 3D element,

makes the STT very efficient at the edges of the cylinder and excites edge precession modes with large magnitude and high frequency. These play a key role in the reversal, inducing in particular a quick and linear decrease of longitudinal magnetic moment versus time instead of the long incubation stage in a flat cell, which is liable to accelerate magnetisation reversal. We believe that our results are meaningful when optimizing perpendicular-shape-anisotropy MRAM cells, and beyond, should be applicable to many situations in the emerging field of 3D spintronics.

ACKNOWLEDGMENTS

The authors would like to thank Liliana Buda-Prejbeanu, Mairbek Chshiev, Ricardo Sousa and Nuno Caçoilo for fruitful discussions and proofreading of the manuscript. This work has been partially supported by the ANR project M-bed-RAM ANR-23-CE24-0016.

-
- [1] A. Fernández-Pacheco, R. Streubel, O. Fruchart, R. Hertel, P. Fischer, and R. P. Cowburn, *Nature Communications* **8** (2017), 10.1038/ncomms15756.
- [2] R. Streubel, E. Y. Tsybal, and P. Fischer, *Journal of Applied Physics* **129** (2021), 10.1063/5.0054025.
- [3] T. Ono, H. Miyajima, K. Shigeto, K. Mibu, N. Hosoi, and T. Shinjo, *Science* **284**, 468 (1999).
- [4] A. V. Chumak, V. I. Vasyuchka, A. A. Serga, and B. Hillebrands, *Nature Physics* **11**, 453 (2015).
- [5] D. Raftrey, A. Hierro-Rodriguez, A. Fernandez-Pacheco, and P. Fischer, *Journal of Magnetism and Magnetic Materials* **563**, 169899 (2022).
- [6] E. C. Burks, D. A. Gilbert, P. D. Murray, C. Flores, T. E. Felter, S. Charnvanichborikarn, S. O. Kucheyev, J. D. Colvin, G. Yin, and K. Liu, *Nano Letters* **21**, 716 (2020).
- [7] F. Meng, C. Donnelly, L. Skoric, A. Hierro-Rodriguez, J.-w. Liao, and A. Fernández-Pacheco, *Micromachines* **12**, 859 (2021).
- [8] N. Perrissin, S. Lequeux, N. Strelkov, A. Chavent, L. Vila, L. D. Buda-Prejbeanu, S. Auffret, R. C. Sousa, I. L. Prejbeanu, and B. Dieny, *Nanoscale* **10**, 12187 (2018).
- [9] K. Watanabe, B. Jinnai, S. Fukami, H. Sato, and H. Ohno, *Nature Communications* **9** (2018), 10.1038/s41467-018-03003-7.
- [10] J. Igarashi, B. Jinnai, K. Watanabe, T. Shinoda, T. Funatsu, H. Sato, S. Fukami, and H. Ohno, *npj Spintronics* **2** (2024), 10.1038/s44306-023-00003-2.
- [11] N. Fernandes-Cacoilo, I. Prejbeanu, O. Fruchart, D. Diény, and R. Sousa, “patent wo2024094571,” (2023).
- [12] N. Caçoilo, S. Lequeux, B. Teixeira, B. Dieny, R. Sousa, N. Sobolev, O. Fruchart, I. Prejbeanu, and L. Buda-Prejbeanu, *Physical Review Applied* **16**, 024020 (2021).
- [13] A. A. Timopheev, R. Sousa, M. Chshiev, L. D. Buda-Prejbeanu, and B. Dieny, *Physical Review B* **92**, 104430 (2015).
- [14] J.-C. Toussaint, “feellgood – a fem micromagnetic simulator,” (2025), accessed: 2025-02-26.
- [15] C. Mattiussi, *Journal of Computational Physics* **133**, 289 (1997).
- [16] N. Fallah, C. Bailey, M. Cross, and G. Taylor, *Applied Mathematical Modelling* **24**, 439 (2000).
- [17] C. Geuzaine and J. Remacle, *International Journal for Numerical Methods in Engineering* **79**, 1309 (2009).
- [18] H. Si and K. Gärtner, *International Journal for Numerical Methods in Engineering* **85**, 1341 (2010).
- [19] S. Rebay, *Journal of Computational Physics* **106**, 125 (1993).
- [20] H. Szabolcs, J.-C. Toussaint, L. Buda-Prejbeanu, F. Alouges, E. Kritisikis, and O. Fruchart, *IEEE Transactions on Magnetics* **44**, 3153 (2008).
- [21] E. Kritisikis, A. Vaysset, L. Buda-Prejbeanu, F. Alouges, and J.-C. Toussaint, *Journal of Computational Physics* **256**, 357 (2014).
- [22] F. Alouges, E. Kritisikis, J. Steiner, and J.-C. Toussaint, *Numerische Mathematik* **128**, 407 (2014).
- [23] J. Slonczewski, *Journal of Magnetism and Magnetic Materials* **159**, L1–L7 (1996).
- [24] S. Zhang and Z. Li, *Physical Review Letters* **93**, 127204 (2004).
- [25] W. Zhang, V. Vlaminc, J. E. Pearson, R. Divan, S. D. Bader, and A. Hoffmann, *Applied Physics Letters* **103** (2013), 10.1063/1.4848102.
- [26] M. Sturma, C. Bellegarde, J.-C. Toussaint, and D. Gusakova, *Physical Review B* **94**, 104405 (2016).
- [27] T. Valet and A. Fert, *Physical Review B* **48**, 7099 (1993).
- [28] M. E. Schabes and H. N. Bertram, *Journal of Applied Physics* **64**, 1347 (1988).
- [29] W. Rave, K. Ramstöck, and A. Hubert, *Journal of Magnetism and Magnetic Materials* **183**, 329 (1998).

- [30] V. V. Slastikov, *Proceedings of the Royal Society A: Mathematical, Physical and Engineering Sciences* **466**, 3167 (2010).
- [31] A. Thiaville, Y. Nakatani, J. Miltat, and Y. Suzuki, *Europhysics Letters (EPL)* **69**, 990 (2005).
- [32] J. Z. Sun, *Physical Review B* **62**, 570 (2000).
- [33] D. Bedau, H. Liu, J.-J. Bouzagloul, A. D. Kent, J. Z. Sun, J. A. Katine, E. E. Fullerton, and S. Mangin, *Applied Physics Letters* **96**, 022514 (2010).
- [34] Y. Takeuchi, H. Sato, S. Fukami, F. Matsukura, and H. Ohno, *Applied Physics Letters* **107** (2015), 10.1063/1.4933256.
- [35] C. Kittel, *Physical Review* **73**, 155 (1948).
- [36] A. S. Arrott, B. Heinrich, and A. Aharoni, *IEEE Transactions on Magnetic* **15**, 1228 (1979).
- [37] A. Thiaville, J. M. García, R. Dittrich, J. Miltat, and T. Schrefl, *Physical Review B* **67**, 094410 (2003).
- [38] A. Ruiz-Calaforra, A. Purbawati, T. Brächer, J. Hem, C. Murapaka, E. Jiménez, D. Mauri, A. Zeltser, J. A. Katine, M.-C. Cyrille, L. D. Buda-Prejbeanu, and U. Ebels, *Applied Physics Letters* **111** (2017).